Novel Electroforming-Free Nanoscaffold Memristor with Very High Uniformity, Tunability, and Density

*Shinbuhm Lee, Abhijeet Sangle, Ping Lu, Aiping Chen, Wenrui Zhang, Jae Sung Lee, Haiyan Wang, Quanxi Jia, and Judith L. MacManus-Driscoll**

Dynamical tuning of the concentration of defects in oxides provides a route to controlling new functionalities.[1] The chemical potential to capture the functionalities driven by mobile ions and defects can be one of the key control parameters (as well as electric field, magnetic field, and stress) for tuning the functionality of complex oxides.[1] Interesting signatures related to oxygen vacancies have been explicitly observed in widespread physical applications, including solid oxide fuel cells,[2] catalysts,[3] optoelectronics,[4] and electronics.[5–14]

In the virgin state of most single-phase oxides (either binary or ternary oxides), the concentration of oxygen vacancies ($V_o^{\cdot\cdot}$ in the notation of Kröger and Vink[8]) is probably not enough to give 'ionotronic' (ionic + electronic) behavior. Depending on the device structures and applications, different approaches have been proposed to increase the $V_o^{\cdot\cdot}$ concentration of oxides in virgin samples. For example, irreversible electroforming is usually required to generate percolating oxygen deficient phases with application of a high electrical stimulus to single-phase oxides (**Figure 1**a).[15,16] Since this electroforming is random and uncontrollable, the variation of device performance across the chip and from-chip-to-chip has been a formidable technical challenge.[12] In addition, since electroforming is destructive, it frequently damages or even kills the devices,[16] and presents very serious obstacles for practical devices. Another method to increase $V_o^{\cdot\cdot}$ in single-phase oxide materials is partial substitution (Figure 1b) with dopants (*e.g.* Y-doped ZrO_2 and Gd-doped CeO_2).[2] This method has been mainly used in oxide electrolytes working at very high temperature for solid oxide fuel cells and oxygen sensors. Higher mobility $V_o^{\cdot\cdot}$ has been reported in lateral multilayers (Figure 1c).[17] Oxygen disorder is observed at the lateral semicoherent heterointerfaces of dissimilar structures, thus providing large concentrations of $V_o^{\cdot\cdot}$ distributed throughout lateral interfaces. However, it is difficult to adapt the lateral multilayers to circuit elements because the current flows in lateral directions, which results in inherently poor integration density. The artificial engineering of $V_o^{\cdot\cdot}$ in ionotronic devices working at room temperature is still in the early stages.

Here, in very simple, self-assembled nanoscaffold films containing nanocolumns with ~10-nm-radius and ~10-nm-intercolumnar-spacing, we demonstrate electroforming-free reversible electroresistance at room temperature. The nanoscaffold films (Figure 1d) are very easy-to-grow, since they self-assemble to give vertical heterointerfaces with $V_o^{\cdot\cdot}$ channels along the interfaces. The structure has a clear advantage over conventional multilayers in multifunctional device nanoengineering.[7,18–21] Our strategy is to design vertical interfaces using two structurally incompatible oxides, which are likely to generate a high concentration $V_o^{\cdot\cdot}$. The resistance variations exceeded two orders of magnitude, with excellent uniformity and tunability. Using electron energy loss spectroscopy, we find oxygen deficiency at the vertical heterointerfaces of nanocolumns and matrix, arising from structural incompatibility. Using conductive atomic force microscopy, we find that high conductivity is confined at vertical heterointerfaces, potentially leading to terabit integration density. Using numerical simulations, we explain the electroresistance in nanoscaffold films by the Joule-heating-accelerated drift of oxygen vacancies localized at vertical heterointerfaces.

We grew nanoscaffold films of $SrTiO_3$-Sm_2O_3, $BaTiO_3$-Sm_2O_3, and $Ba_{0.6}Sr_{0.4}TiO_3$-Sm_2O_3 onto (001) Nb-doped $SrTiO_3$ substrates using a simple one-step process of pulsed laser deposition. The cubic bixbyite Sm_2O_3 is an ideal material because it substitutes only minimally into alkaline earth titanate perovskites.[19–21] **Figure 2**a shows the nonvolatile resistance (R) switching as a function of voltage (V) in nanoscaffold $SrTiO_3$-Sm_2O_3 films, whose electrodes are circular Pt with 50-μm-radius. For all the electrical measurements, we grounded the Nb-doped $SrTiO_3$ substrate and applied the voltage to the Pt electrodes. The films were highly resistive (~10 MΩ) in their virgin state. To switch

Dr. S. Lee, A. Sangle, Prof. J. L. MacManus-Driscoll
Department of Materials Science and Metallurgy
University of Cambridge
27 Charles Babbage Road, Cambridge, CB3 0FS, UK
E-mail: jld35@cam.ac.uk
Dr. P. Lu
Sandia National Laboratories
Albuquerque, New Mexico 87185, USA
W. Zhang, Prof. H. Wang
Department of Electrical and Computer Engineering
Texas A&M University
College Station
Texas 77843, USA
Dr. J. S. Lee
School of Physics
Korea Institute for Advanced Study
Seoul 130–722, Republic of Korea
Dr. A. Chen, Dr. Q. X. Jia
Center for Integrated Nanotechnologies
Los Alamos National Laboratory
Los Alamos, New Mexico 87545, USA

DOI: 10.1002/adma.201401917

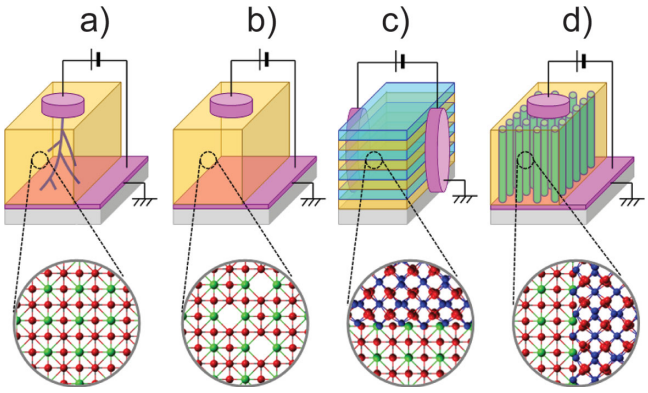

Figure 1. Schematic diagrams of conventional methods to generate $V_o^{\cdot\cdot}$. a) Irreversible electroforming with application of a high electrical stimulus to single-phase oxides. b) Conventional single-phase oxide film fractionally substituted with dopants. c) Conventional multilayer film causing oxygen disorder at the lateral heterointerfaces of dissimilar crystal structures. d) Nanoscaffold film causing oxygen vacancies at the vertical heterointerfaces of dissimilar crystal structures.

the resistance value, we applied sequential voltage pulses, with amplitude increasing or decreasing with time. To read the resistance value between each voltage pulse, +0.1 V was applied and the current was measured. When we applied a small positive voltage, the virgin state was switched into low-resistance state (LRS). When we applied a small negative voltage, the device in the LRS could be switched back into the high-resistance state (HRS). Similar *R*–*V* curves were also observed in other nanoscaffold $Ba_{0.6}Sr_{0.4}TiO_3$-Sm_2O_3 and $BaTiO_3$-Sm_2O_3 films (Figure S1).

It should be noted that we could obtain a broad range of intermediate resistance states since the resistance switching occurs gradually. The inner concentric loops in Figure 2a (black to blue curves) show that the ratio of high and low resistances can be finely tuned, depending on the amplitude of applied voltage. For example, resistance ratios of LRS and HRS were ~100 (black curve) and ~10 (green curve) when we applied $|V|$ of 10 V and 5 V, respectively. The phenomenon has recently been attracted great attentions to realize multilevel data storage memory (so-called memristor).[8–13]

Interestingly, the nonlinear electroresistance occurs without destructive electroforming in the nanoscaffold devices. Indeed, the resistance of HRS (~10 MΩ) is very similar to that of the virgin state even after many repeated electrical cycles (Figure S2). The resistance values of both LRS and HRS scaled inversely with the electrode area, indicating that the conduction pathways are uniformly distributed. On the contrary, electroforming was present in single $SrTiO_3$ and Sm_2O_3 films, since the current increased suddenly when we applied a voltage in their virgin state (Figure S3).

The electroresistance in the electroforming-free nanoscaffold films was superior to electroforming single-phase oxides in following aspects. First, the resistance variation with repeated electrical cycles (i.e., endurance) is very uniform in our nanoscaffold films. We applied sequential voltage pulses of +10 V and –10 V to switch the resistance state and +0.1 V between each voltage pulse to read the resistance. The excellent uniform resistance variations last for over 10^3-cycles, as shown by a black line in Figure 2b. After one month, we found that the device had retained the original resistance state without obvious degradation (long retention, Figure S4). As shown by the grey line, the device still reveals excellent uniform resistance variations over 10^6 cycles with a similar resistance ratio. In addition, the uniform endurance and the nonvolatile *R*–*V* curves are reproducible from device to device (Figure S5). Second, the resistances of HRS and LRS are tunable by varying deposition conditions. Figure 2c and d show large variations of resistance with orders of magnitude change when we varied either the film thickness or the laser repetition rate during film deposition, respectively. We can easily obtain a resistance corresponding to an optimum current level (e.g., ~1 μA) for both low power consumption and reliable information sensing. As pointed out in other reports,[12,22]

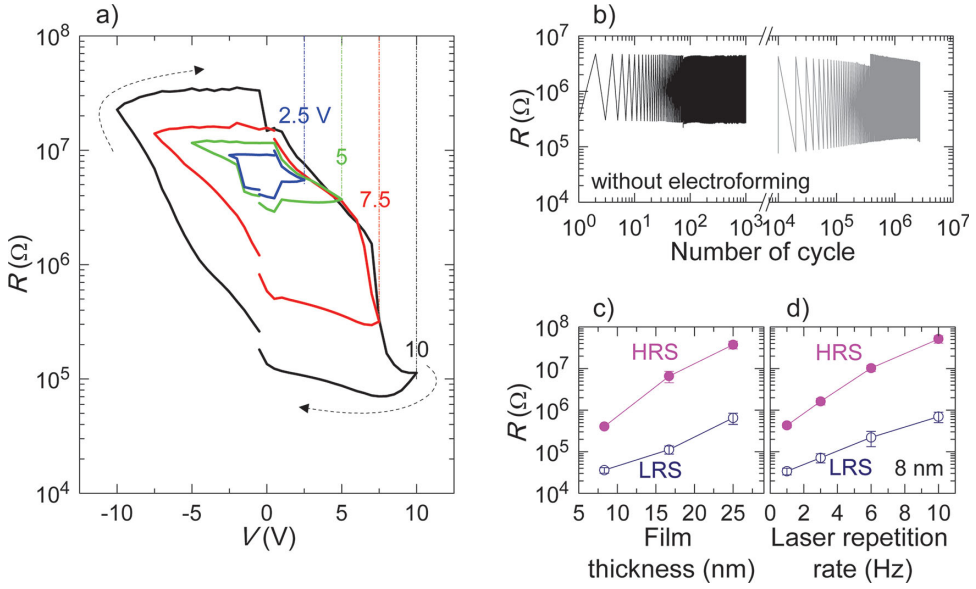

Figure 2. Electroresistance of $SrTiO_3$-Sm_2O_3 nanoscaffold device. a) Multilevel *R*–*V* curves. b) Very uniform resistance variation with repeated electrical cycles. c) and d) Systematic tunable resistances of HRS and LRS by varying film thickness and laser repetition rate.

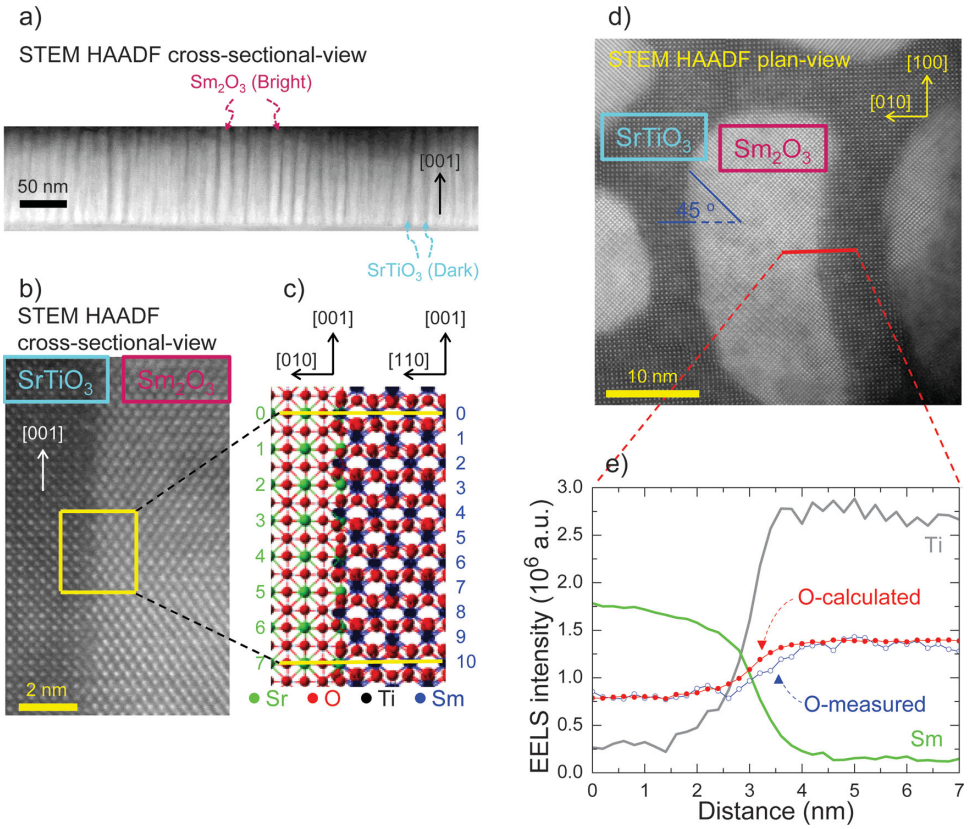

Figure 3. Formation of $V_o^{\cdot\cdot}$ at vertical heterointerfaces due to the structural discontinuity of $SrTiO_3$ matrix and Sm_2O_3 nanocolumn. a) "Nano-comb"-like spontaneous phase ordering in cross-sectional-view of nanoscaffold $SrTiO_3$-Sm_2O_3, as revealed by cross-sectional STEM HAADF image. b) High-resolution HAADF image of vertical interface of $SrTiO_3$ matrix and Sm_2O_3 nanocolumn in cross-sectional-view. c) Crystallographic modelling of vertical interface between $SrTiO_3$ and Sm_2O_3. d) STEM HAADF plan-view image of $SrTiO_3$ matrix and Sm_2O_3 nanocolumn. e) Measured concentration profile of Sm (green line), Ti (grey line) and O (blue circles) elements across the vertical interface using EELS. Shown in red circles is the calculated EELS signal of O element.

the simultaneous realization of the above-mentioned properties in the same device was the most difficult problem in single-phase oxide films due to the requirement of electroforming. To the best of our knowledge, our nanoscaffold devices are the first to give electroforming-free behavior in a simple device along nano-engineered ionic channels.

To explore the possible origin of the intriguing, new non-linear electroresistance phenomenon we have observed in the nanoscaffold films, we investigated the atomic structure at the vertical interfaces. **Figure 3**a is a scanning transmission electron microscopy (STEM) high-angle annular dark-field (HAADF) image of nanoscaffold $SrTiO_3$-Sm_2O_3 films in cross-sectional-view, showing spontaneous phase ordering. The 100-nm-long bright nanocolumns are very straight. The dark and bright contrast regions of ~10-nm-width are alternatively separated like a "nano-comb". Due to atomic number *Z*-contrast nature of HAADF imaging, the dark and bright areas in the image correspond to the $SrTiO_3$ and Sm_2O_3, respectively. The result was further confirmed by energy-dispersive x-ray spectroscopy (EDS) (Figure S6). The epitaxial Sm_2O_3 phase grows on the Nb-doped $SrTiO_3$ substrate with a 45° in-plane rotation to minimize their lattice mismatch,[19–21] which was also proven by an x-ray diffraction phi-scan (Figure S7). The reciprocal space maps also reveal that the $(0\bar{4}8)$ Sm_2O_3 peak of $SrTiO_3$-Sm_2O_3 nanoscaffold films is much narrower than that of single Sm_2O_3 films (Figure S8). This indicates that, in the nanoscaffold film, both Sm_2O_3 and $SrTiO_3$ are well crystallized and their lattice constants are uniform through the thickness of the film.[19–21]

Now, we consider structural incompatibility at the vertical interfaces of $SrTiO_3$ and Sm_2O_3. Figure 3b shows a high-resolution HAADF image of the vertical interfaces in cross-sectional-view. This atomic resolution image indicates sharp interface between $SrTiO_3$ and Sm_2O_3. According to schematic crystallographic modeling in Figure 3c, every 11th Sm atomic plane can match with the SrO layer of every 8th consecutive $SrTiO_3$ unit cell because $10\times a_{Sm_2O_3} \approx 7\times a_{SrTiO_3}$ (≈27 Å), where $a_{Sm_2O_3}$(≈2.7 Å) and a_{SrTiO_3} (≈3.9 Å) correspond to interplanar spacing of the Sm_2O_3 (004) and $SrTiO_3$ (001) planes, respectively. This partial lattice matching is energetically favorable because the residual strain could be significantly reduced.[21] However, between matching planes, the vertical interfaces should be structurally incompatible due to large lattice misfit and different atomic patterns of $SrTiO_3$ (perovskite, $Pm\bar{3}m$ in the notation of the space group) and Sm_2O_3 (bixbyite, $Ia\bar{3}$). Hence, misfit dislocations should exist at the vertical interfaces, leading to higher density $V_o^{\cdot\cdot}$.[23,24]

Considering the structural incompatibility at the vertical interface of the $SrTiO_3$ matrix and the Sm_2O_3 nanocolumns, we propose that a large concentration of $V_o^{\cdot\cdot}$ can readily form there. To check this hypothesis, we measured the concentration profile of atomic elements across the vertical interface by

the electron energy loss spectroscopy (EELS). Figure 3e shows corresponding EELS signals along a red line across Sm_2O_3-$SrTiO_3$ interface in STEM HAADF plan-view image of Figure 3d. As expected, the EELS signals of Sm (green line) and Ti (grey line) elements are much stronger inside the Sm_2O_3 nanocolumn and the $SrTiO_3$ matrix, respectively. The most important discovery from this measurement is the observation of oxygen deficiency right across the vertical interface. For example, we observed that the EELS signals of Sm, Ti and O (blue circles) change steadily within ~2-nm-wide interface region. To check the oxygen deficiency, we calculated the EELS signal of O using the EELS signals of Ti and Sm, assuming a stoichiometric O condition, i.e., O/Ti = 3 and O/Sm = 1.5 for $SrTiO_3$ and Sm_2O_3, respectively. The calculated O EELS signals were fitted to the experimental O EELS signals in areas deeper inside $SrTiO_3$ matrix and Sm_2O_3 nanocolumn, respectively. The calculated EELS signal of O (red circles) matches well with the measured values deeper inside the nanocolumns and the matrix in Figure 3e. However, close to the interface, the calculated EELS signal of O is higher than the measured value, indicating oxygen deficiency at the vertical interface.

To extract local information about the current flow path through the nanoscaffold $SrTiO_3$-Sm_2O_3 films, we recorded a current–voltage (I–V) curve using conductive atomic force microscopy with high lateral resolution. Unlike multilayers where interfaces are buried (Figure 1c), in nanoscaffold structure the interfaces are accessible from the electrical contact[25] and so we can easily probe the physical properties of the vertical interfaces. To distinguish between the interface and the nanocolumn of the studied sample, we first acquired the surface topography, as shown in the inset of **Figure 4**a. We then placed the Pt-coated tip at positions on the interface and on the nanocolumn, and swept the voltage from –10 V to 10 V in spectroscopic mode to record I–V curves at each position. As clearly shown in Figure 4a, the high conductivity is detected only at the interface (triangles), while both nanocolumn (squares) and matrix are insulating. In addition, we compared the conductance of the nanoscaffold $SrTiO_3$-Sm_2O_3 film with that of single $SrTiO_3$ and Sm_2O_3 films in the 20 to 550 °C temperature range. As shown in Figure 4b, the nanoscaffold $SrTiO_3$-Sm_2O_3 films (circles) show a markedly increased conductance for the entire temperature range, compared to the single $SrTiO_3$ (triangles) and Sm_2O_3 (squares) films. Both results indicate that a high concentration of $V_o^{\cdot\cdot}$ along the vertical interfaces can result in local current flow paths. Considering the narrow interfaces of ~2-nm-width, the resistive switching behavior illustrated in nanoscaffold structures can potentially lead to a memory density of 40 Tb/in^2.

To gain insights into the physical mechanism responsible for electroresistance in nanoscaffold devices, we analysed the dynamics of high-to-low resistance switching. We measured the resistance variation $R(t)$ by applying the voltage pulse with a constant amplitude of V_p linearly over time t. For example, when we applied +0.5 V, the $R(t)$ of HRS decreased gradually, as shown in Figure 4c. Just as for other transient phenomena,[26,27] we can fit $R(t)$ nicely using a stretched exponential law, i.e., $R(t) = R(0)\exp[-(t/\tau)^{\alpha}]$, where α and τ represent the numeric exponent and the transient time, respectively. Figure 4d shows a thermally activated behavior of τ when we changed temperature from 18 to 70 °C. It should be noted that the activation energy U of τ was determined to be 1.1 ± 0.1 eV, based on an Arrhenius plot of $1/\tau$. The value of 1.1 eV agrees well with the activation energy of $V_o^{\cdot\cdot}$,[8,26,27] suggesting that the drift of $V_o^{\cdot\cdot}$ dominates the high-to-low resistance switching in our nanoscaffold devices.

We found that τ decreased by more than seven orders of magnitude, when we increased V_p linearly within 10 V, as shown in Figure 4e. Different from the planar structure of FLASH memory, the writing/erasing and reading can take place in the same direction due to the vertical geometry of the devices, possibly disturbing the data storage by the reading operation. However, this so-called voltage-time dilemma can be overcome when their operating times behave nonlinearly to the operating stimuli.[27] The nanoscaffold device represents this case due to the significant nonlinearity of the V_p-τ relationship. Interestingly, the nonlinearity of the V_p-τ relationship becomes much steeper with just a slight decrease of film thickness. From the measured data of the 8-nm-thick device, we found that τ decreases by nine orders of magnitude within 6 V. To understand this dependence quantitatively, we calculated τ by considering the Joule-heating-accelerated drift of $V_o^{\cdot\cdot}$ (see Supporting Information for details). As displayed by the solid lines, the calculated τ-values are in good agreement with the measured ones. These results clearly show a significant role of drift of $V_o^{\cdot\cdot}$ on the electroresistance in the nanoscaffold devices.

Overall, the observed electroresistance in nanoscaffold film can be explained by the modulation of the interfacial electronic barrier due to the migration of $V_o^{\cdot\cdot}$. Due to the high concentration of oxygen vacancies, the $SrTiO_3$-Sm_2O_3 vertical interface regions belong to the class of n-type semiconducting oxides.[8,10] The contact of Pt and n-type semiconducting oxide typically forms Schottky-like barrier due to high-work-function of the Pt metals. The asymmetric I–V curves in Figure S2 supports this Schottky-barrier formation. Since the bottom interface with Nb-doped $SrTiO_3$ substrate in an Ohmic contact, the major contribution for the electroresistance will come from the upper interface. When $V_o^{\cdot\cdot}$, produced at the $SrTiO_3$-Sm_2O_3 vertical interfaces, are attracted toward the upper interface with application of a negative voltage and are concentrated near the upper interface, the remaining region becomes $V_o^{\cdot\cdot}$-deficient.[28,29] As the $V_o^{\cdot\cdot}$-deficient region becomes wider, the interfacial electronic barrier is widened, causing the device to go into the HRS. When $V_o^{\cdot\cdot}$ move away from the upper interface with application of a positive voltage, the width of the $V_o^{\cdot\cdot}$-deficient region is narrowed and the interfacial electronic barrier is narrowed, causing the device to go into the LRS.

In conclusion, we have developed easy-to-grow nanoscaffold devices showing extraordinary field-dependent electroresistance at room temperature, using $V_o^{\cdot\cdot}$ localized at vertical heterointerfaces. The resistance variations exceed two orders of magnitude with very high uniformity and tunability. Using EELS, we found that oxygen deficient regions are readily confined at the vertical interface of the nanocolumns and the matrix, due to the structural incompatibility of dissimilar oxides. Regularly distributed and spatially confined $V_o^{\cdot\cdot}$ present in our films minimize the stray conduction channels, which are responsible for non-uniformity and non-reproducibility in single-phase oxides. The $V_o^{\cdot\cdot}$ engineering at the nanoscale by means of nanoscaffold structures spatially confines the conduction channels at vertical interfaces and gives better control over the device performance with high

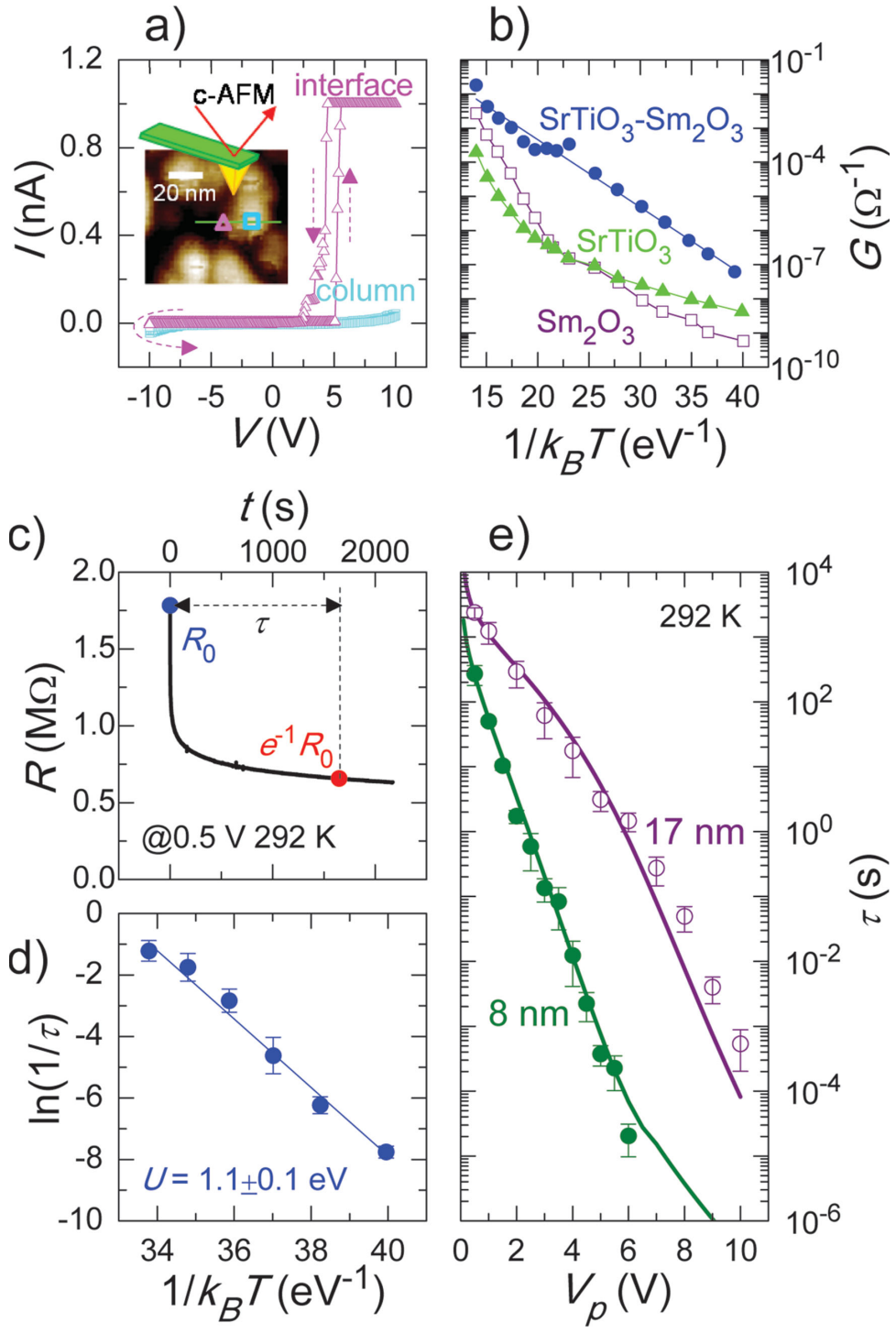

Figure 4. Local conduction of thermally activated $V_o^{\cdot\cdot}$ at the vertical heterointerface of $SrTiO_3$ matrix and Sm_2O_3 nanocolumn. a) *I*–*V* curves at interface (triangles) and inside nanocolumn (squares) using conductive AFM. The inset shows the surface topography. b) Conductance of nanoscaffold $SrTiO_3$-Sm_2O_3 film (circles), single $SrTiO_3$ (triangles) and Sm_2O_3 (squares) thin films for *T*-variation from 20 to 550 °C. c) Nonlinear transient times τ for high-to-low resistance switching. d) Thermally activated behavior of τ for *T*-variation from 18 to 70 °C. e) Film thickness dependence of V_p-τ relationship.

uniformity and reproducibility. Our experimental and theoretical approaches provide the fundamental basis for understanding the electroresistance in nanoscaffold devices. These capabilities for exploring and controlling ionically active functionality should lay the basis for ionotronic technologies, e.g. ionic transport, electrochemical phenomena and magneto-electric coupling, in vertical oxide heterointerfaces which may find wide applications in universal devices and clean energy.

Experimental Section

We deposited insulating $SrTiO_3$-Sm_2O_3 nanoscaffold films onto 1 *at.*% Nb-doped $SrTiO_3$ (001) substrates by a simple one-step process of pulsed laser deposition. Although we used a polycrystalline target containing $SrTiO_3$ and Sm_2O_3 of 50:50 weight ratio, the self-assembled growth of $SrTiO_3$ and Sm_2O_3 is expected, as schematically shown in Figure 1d. The growth of $SrTiO_3$-Sm_2O_3 nanoscaffold films can be modeled as a diffusion process.[30] The multicomponent species come to the film surface and phase-separate into nanoscaffold films. We used a KrF laser ($\lambda = 248$ nm) with a fluence of 1.5 J/cm^2 and a repetition rate of 1–10 Hz. The films were grown at a substrate temperature of 800 °C and an oxygen pressure of 0.2 mbar. Film thicknesses were in the range of 8–125 nm. The samples were post-annealed at 650 °C for 1 hour under 400 mbar O_2 to assure proper oxygen stoichiometry and to minimize the oxygen vacancies inside films. Circular Pt electrodes of 50-μm-radius defined by shadow masks were sputter coated onto the $SrTiO_3$-Sm_2O_3 nanoscaffold films. To fabricate nanoscaffold $Ba_{0.6}Sr_{0.4}TiO_3$-Sm_2O_3 and $BaTiO_3$-Sm_2O_3 films, we underwent the same deposition procedure using polycrystalline targets containing 50:50 *wt.*% mix. We also fabricated single $SrTiO_3$ and Sm_2O_3 films under the same deposition procedure using $SrTiO_3$ and Sm_2O_3 polycrystalline targets, respectively.

Supporting Information

Supporting Information is available from the Wiley Online Library or from the author.

Acknowledgements

This work was supported by the European Research Council (ERC) (Advanced Investigator grant ERC-2009-AdG-247276-NOVOX), the UK Engineering and Physical Sciences Research Council (EPSRC) and the US National Science Foundation (grant no. NSF-1007969). The work at Los Alamos National Laboratory was supported by an LDRD program and performed, in part, at the Centre for Integrated Nanotechnologies, a U.S. Department of Energy and Office of Basic Energy Sciences user facility. Sandia National Laboratories is a multi-program laboratory managed and operated by Sandia Corporation, a wholly owned subsidiary of Lockheed Martin Corporation, for the US Department of Energy's National Nuclear Security Administration under contract DE-AC04–94AL85000. Part of the TEM and STEM work at Texas A&M University was supported by the U.S. National Science Foundation (DMR Ceramic Program, NSF-1007969). A.S. and J.S.L. acknowledge financial support from the Cambridge Commonwealth Trust and the National Research Foundation of Korea (Grant No. 2011- 35B-C00014), respectively.

Received: April 28, 2014
Revised: June 28, 2014
Published online: July 28, 2014

[1] S. V. Kalinin, N. A. Spaldin, *Science* **2013**, *341*, 858.
[2] E. D. Wachsman, K. T. Lee, *Science* **2011**, *334*, 935.
[3] H. Jeen, W. S. Choi, M. D. Biegalski, C. M. Folkman, I-C. Tung, D. D. Fong, J. W. Freeland, D. Shin, H. Ohta, M. F. Chisholm, H. N. Lee, *Nat. Mater.* **2013**, *12*, 1057.
[4] D. Kani, T. Terashima, R. Kanda, A. Masuno, K. Tanaka, S. Chu, H. Kan, A. Ishizumi, Y. Kanemitsu, Y. Shimakawa, M. Takano, *Nat. Mater.* **2005**, *4*, 816.
[5] C.-H. Yang, J. Seidel, S. Y. Kim, P. B. Rossen, P. Yu, M. Gajek, Y. H. Chu, L. W. Martin, M. B. Holcomb, Q. He, P. Maksymovych, N. Balke, S. V. Kalinin, A. P. Baddorf, S. R. Basu, M. L. Scullin, R. Ramesh, *Nat. Mater.* **2009**, *8*, 485.
[6] J. Jeong, N. Aetukuri, T. Graf, T. D. Schladt, M. G. Samant, S. S. P. Parkin, *Science* **2013**, *339*, 1402.
[7] T. Fix, E.-M. Choi, J. W. A. Robinson, S. Lee, A. P. Chen, B. Prasad, H. Wang, M. G. Blamire, J. L. MacManus-Driscoll, *Nano Lett.* **2013**, *13*, 5886.
[8] R. Waser, R. Dittmann, G. Staikov, K. Szot, *Adv. Mater.* **2009**, *21*, 2632.
[9] D. B. Strukov, G. S. Snider, D. R. Stewart, R. S. Williams, *Nature* **2008**, *453*, 80.
[10] J. J. Yang, M. D. Pickett, X. Li, D. A. A. Ohlberg, D. R. Stewart, R. S. Williams, *Nat. Nanotechnol.* **2008**, *3*, 429.
[11] M.-J. Lee, C. B. Lee, D. Lee, S. R. Lee, M. Chang, J. H. Hur, Y.-B. Kim, C.-J. Kim, D. H. Seo, S. Seo, U-I. Chung, I.-K. Yoo, K. Kim, *Nature Mater.* **2011**, *10*, 625.
[12] J. J. Yang, D. B. Strukov, D. R. Stewart, *Nat. Nanotechnol.* **2013**, *8*, 13.
[13] J. Borghetti, G. S. Snider, P. J. Kuekes, J. J. Yang, D. R. Stewart, R. S. Williams, *Nature* **2010**, *464*, 873.
[14] M. D. Pickett, G. Medeiros-Ribeiro, R. S. Williams, *Nat. Mater.* **2013**, *12*, 114.
[15] J. P. Strachan, M. D. Pickett, J. J. Yang, S. Aloni, A. L. D. Kilcoyne, G. Medeiros-Ribeiro, R. S. Williams, *Adv. Mater.* **2010**, *22*, 3573.
[16] J. J. Yang, F. Miao, M. D. Pickett, D. A. A. Ohlberg, D. R. Stewart, C. N. Lau, R. S. Williams, *Nanotechnology* **2009**, *20*, 215201.
[17] J. Garcia-Barriocanal, A. Rivera-Calzada, M. Varela, Z. Sefrioui, E. Iborra, C. Leon, S. J. Pennycook, J. Santamaria, *Science* **2008**, *321*, 676.
[18] H. Zheng, J. Wang, S. E. Lofland, Z. Ma, L. Mohaddes-Ardabili, T. Zhao, L. Salamanca-Riba, S. R. Shinde, S. B. Ogale, F. Bai, D. Viehland, Y. Jia, D. G. Schlom, M. Wuttig, A. Roytburd, R. Ramesh, *Science* **2004**, *303*, 661.
[19] J. L. Macmanus-Driscoll, P. Zerrer, H. Wang, H. Yang, J. Yoon, A. Fouchet, R. Yu, M. G. Blamire, Q. X. Jia, *Nat. Mater.* **2008**, *7*, 314.
[20] S. A. Harrington, J. Zhai, S. Denev, V. Gopalan, H. Wang, Z. Bi, S. A. T. Redfern, S.-H. Baek, C. W. Bark, C.-B. Eom, Q. X. Jia, M. E. Vickers, J. L. MacManus-Driscoll, *Nat. Nanotechnol.* **2011**, *6*, 491.
[21] O. J. Lee, S. A. Harrington, A. Kursumovic, E. Defay, H. Wang, Z. Bi, C.-F. Tsai, L. Yan, Q. X. Jia, J. L. MacManus-Driscoll, *Nano Lett.* **2012**, *12*, 4311.
[22] International Technology Roadmap for Semiconductors (ITRS). Emerging Research Devices. ITRS technical report 2012, http://www.itrs.net, accessed: September, **2013**.
[23] C. Korte, A. Peters, J. Janek, D. Hesse, N. Zakharovb, *Phys. Chem. Chem. Phys.* **2008**, *10*, 4623.
[24] M. M. McGibbon, N. D. Browning, M. F. Chisholm, A. J. McGibbon, S. J. Pennycook, V. Ravikumar, V. P. Dravid, *Science* **1994**, *266*, 102.
[25] Y.-H. Hsieh, J.-M. Liou, B.-C. Huang, C.-W. Liang, Q. He, Q. Zhan, Y.-P. Chiu, Y.-C. Chen, Y.-H. Chu, *Adv. Mater.* **2012**, *24*, 4564.
[26] F. Miao, J. J. Yang, J. Borghetti, G. Medeiros-Ribeiro, R. S. Williams, *Nanotechnology* **2011**, *22*, 254007.
[27] S. Menzel, M. Waters, A. Marchewka, U. Böttger, R. Dittmann, R. Waser, *Adv. Funct. Mater.* **2011**, *21*, 4487.
[28] R. Muenstermann, T. Menke, R. Dittmann, R. Waser, *Adv. Mater.* **2010**, *22*, 4819.
[29] J. S. Lee, S. Lee, B. Kahng, T. W. Noh, *Appl. Phys. Lett.* **2013**, *102*, 253503.
[30] H. Zheng, F. Straub, Q. Zhan, P.-L. Yang, W.-K. Hsieh, F. Zavaliche, Y.-H. Chu, U. Dahmen, R. Ramesh, *Adv. Mater.* **2006**, *18*, 2747.